日本磁気学会
ISSN 2432-0250
Journal of the Magnetics Society of Japan
Electronic Journal URL: https://www.jstage.jst.go.jp/browse/msjmag

Vol.45 No.1　2021

Journal

JOURNAL OF THE MAGNETICS SOCIETY OF JAPAN

Vol.45 No.1 2021

日本磁気学会

ISSN 2432-0250

HP: http://www.magnetics.jp/ e-mail: msj@bj.wakwak.com

Electronic Journal: http://www.jstage.jst.go.jp/browse/msjmag

世界初！
高温超電導型VSM

新製品

世界初*、高温超電導マグネットをVSMに採用することで
測定速度 当社従来機1/20を実現。
0.5mm cube磁石のBr, HcJ高精度測定が可能と
なりました。
*2014年7月 東英工業調べ

測定結果例

高温超電導VSMによるNdFeB(sint.) 0.5mm cube BHカーブ

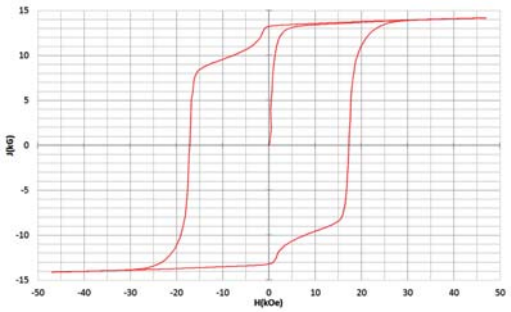

磁化測定レンジ：0.2emu
Br = 13.2kG　　HcJ = 17.2kOe

高温超電導VSMによるNdFeB(sint.) 1mm cube BHカーブ

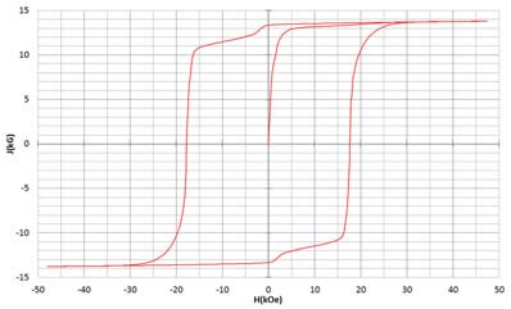

磁化測定レンジ：2emu
Br = 13.3kG　　HcJ = 17.7kOe

高温超電導VSMによるNdFeB(sint.) 4mm cube BHカーブ

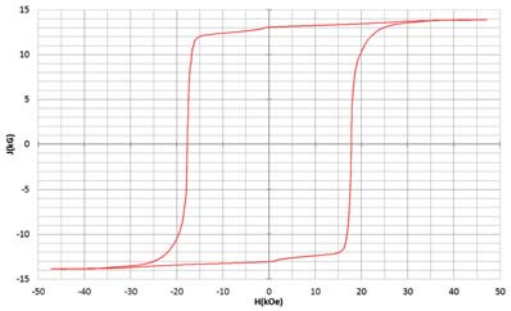

磁化測定レンジ：100emu
Br = 13.1kG　　HcJ = 17.8kOe

高速測定を実現

高温超電導マグネット採用により、高速測定を実現しました。Hmax= 5Tesla, Full Loop 測定が2分で可能です。
（当社従来機：Full Loop測定　40分）

小試料のBr,HcJ高精度測定

0.5mm cube 磁石のBr,HcJ高精度測定ができ、表面改質領域を切り出しBr,HcJの強度分布等、微小変化量の比較測定が可能です。
また、試料の加工劣化の比較測定が可能です。

試料温度可変測定

−50℃～+200℃温度可変UNIT（オプション）

磁界発生部の小型化

マグネットシステム部寸法：0.8m×0.3m×0.3m

TOEI 東英工業株式会社
http://www.toeikogyo.co.jp
〒194-0035 東京都町田市忠生1-8-13
TEL：042-791-1211 FAX：042-792-0490
E-mail : sales@toeikogyo.co.jp

Journal of the Magnetics Society of Japan
Vol. 45, No. 1

Electronic Journal URL: https://www.jstage.jst.go.jp/browse/msjmag

CONTENTS

J. Magn. Soc. Jpn., **45**, 1-5 (2021)

Letter

Estimation of angular momentum compensation temperature in GdFe film by magnetic Compton scattering

Tetsuya Ikebuchi†, Yuushou Hirata†, Shinsaku Funada, Arata Tsukamoto*,

Haruka Ito**, Kosuke Suzuki**, Kazushi Hoshi**, Naruki Tsuji***, Hiroshi Sakurai**,

Yoichi Shiota, Takahiro Moriyama, and Teruo Ono****

Institute for Chemical Research, Kyoto University, *Gokasho Uji, Kyoto 611-0011, Japan*

*College of Science and Technology, Nihon University, *Narashino-dai Funabashi, Chiba 274-8501, Japan*

**Department of Electronics and Informatics, Gunma University, *Tenjin-cho Kiryu, Gunma 376-8515, Japan*

***JASRI, Kouto Sayo-cho, *Hyogo 679-5198, Japan*

****Center for Spintronics Research Network (CSRN), Graduate School of Engineering Science, Osaka University, *Toyonaka, Osaka 560-8531, Japan*

The angular momentum compensation temperature, T_A, in transition metal rare earth (TM-RE) ferrimagnetic materials is a crucial property for utilizing antiferromagnetic spin dynamics, which is much faster than its ferromagnetic counterpart. However, reports on the estimation of T_A in ferrimagnets are limited. In this study, we measured the temperature dependence of the spin magnetization and orbital magnetization of GdFe amorphous perpendicular magnetization film by using magnetic Compton scattering. Then, we estimated T_A experimentally.

Keywords: magnetic Compton scattering, TM-RE ferrimagnets, angular momentum compensation temperature

Antiferromagnets are a promising candidate for the core elements of future spintronic devices because they exhibit ultra-fast spin dynamics and a low magnetic susceptibility to magnetic fields [1)-4)]. These desirable properties originate from the antiferromagnetic ordering, in which the magnetic moments are compensated for on an atomic scale [5)]. However, generally, antiferromagnets are difficult to manipulate and probe due to the small net magnetization and magnetic immunity. Hence, recently, transition metal and rare earth (TM-RE) ferrimagnetic materials, in which two inequivalent magnetic sublattices are antiferromagnetically coupled, have been attracting attention [6)-11)]. This is because these materials have nonzero magnetization, which enables us to manipulate and probe them. These ferrimagnets exhibit two compensation temperatures due to the different Landé g-factors of the TM and RE elements. One is the magnetization compensation temperature, T_M, at which the net magnetic moment vanishes. The other is the angular momentum compensation temperature, T_A, at which the net angular momentum vanishes. Ultra-fast domain wall (DW) motions were demonstrated at T_A in TM-RE ferrimagnets in both field-driven and current-driven cases [12)-17)]. These results suggest that the ferrimagnets exhibit antiferromagnetic spin dynamics at T_A. This is because the time evolution of the state of a magnet is governed by the commutation relation of the angular momentum, not of the magnetic moment. Therefore, the estimation of T_A is a crucial step toward utilizing antiferromagnetic spin dynamics, but reports on this have been limited.

Recently, Imai et al. [18)] reported an angular momentum compensation temperature in a ferrimagnet insulator $Ho_3Fe_5O_{12}$, by using the Barnett effect measurement technique. This measurement is simple, but there is no element specific information, which is important to understanding ferrimagnetic properties. Here, as a pioneering new experimental method, we focus on magnetic Compton scattering. Compton scattering photons reflect the momentum density distribution of the target electron. Experimentally, by irradiating a magnetic substance with circular polarized X-rays, the spin magnetization of magnetically active electrons can be measured. If the system is composed of independent particles described by a single wave function, $\psi_{\sigma_i}(\boldsymbol{r})$ ($\sigma =$ majority spin or minority spin), within the limit of the impulse approximation, we can write the momentum density $n_\sigma(\boldsymbol{p})$ by summing over all occupied single electron states of the system $\chi_{\sigma i}(\boldsymbol{p})$ as follows [19)-21)].

$$n_\sigma(\boldsymbol{p}) = \sum_i^{occ} |\chi_{\sigma i}(\boldsymbol{p})|^2. \quad (1)$$

$$\chi_{\sigma i}(\boldsymbol{p}) = \left(\frac{1}{\sqrt{2\pi\hbar}}\right)^3 \int \psi_{\sigma_i}(\boldsymbol{r})\, exp\left(-\frac{i\boldsymbol{p}\boldsymbol{r}}{\hbar}\right) d\,\boldsymbol{r}. \quad (2)$$

Here, $\boldsymbol{p}\left(=\left(p_x, p_y, p_z\right)\right)$ is the momentum of an electron in a solid, and p_z is the momentum of an electron in the material along the X-ray scattering vector, $\boldsymbol{K}$. The scattering vector is defined as

$$\boldsymbol{K} = \boldsymbol{K_2} - \boldsymbol{K_1}. \quad (3)$$

Here, $\boldsymbol{K_2}$ and $\boldsymbol{K_1}$ denote the wave vectors of incident and Compton scattering X-rays, respectively. A magnetic

Corresponding author:
Hiroshi Sakurai (e-mail: sakuraih@gunma-u.ac.jp).
Teruo Ono (e-mail: ono@scl.kyoto-u.ac.jp).

† These authors contributed equally to this work.

Compton profile, (MCP), $J_{mag}(p_z)$, is given by the following equation.

$$J_{mag}(p_z) = \iint (n_{maj}(\boldsymbol{p}) - n_{min}(\boldsymbol{p}))\mathrm{d}p_x\mathrm{d}p_y. \quad (4)$$

Here, $n_{maj}(\boldsymbol{p})$ ($n_{min}(\boldsymbol{p})$) denotes the momentum density with the majority (minority) spin. Then, the spin magnetic moment, μ_s, is determined from the $J_{mag}(p_z)$ as [19)-20)]

$$\mu_s = \int J_{mag}(p_z)dp_z. \quad (5)$$

Total magnetization M_t, which is measured by a superconducting quantum interference device magnetometer, is expressed as the following.

$$M_t = M_s + M_l. \quad (6)$$

Here, M_s denotes the spin magnetization, which is obtained from a magnetic Compton scattering measurement, and M_l denotes the orbital magnetization. Therefore, it is possible to estimate individual M_t, M_s, and M_l.

In this paper, we focus on a ferrimagnetic GdFe alloy in which Gd and Fe are antiferromagnetically coupled. First, the magnetization compensation temperature T_M is obtained from the temperature dependence of M_t. Next, the magnitudes of the spin magnetizations of Gd and Fe ($M_{s,Gd}$ and $M_{s,Fe}$) in the ferrimagnetic GdFe alloy are measured using magnetic Compton scattering, and the spin magnetization compensation temperature T_S, at which $M_{s,Gd}$ is equal to $M_{s,Fe}$, is determined. Then, assuming that the $M_{l,Gd}$ of Gd is zero, the orbital magnetization $M_{l,Fe}$ of Fe is obtained from the difference between M_t and M_s. Then, the g-factor of Gd and Fe is determined, and finally, the T_A of GdFe alloy is estimated.

GdFe films with a thickness of 1 μm were grown by DC sputtering using Gd and Fe targets on Al film substrates with a thickness of 6 μm as shown in Fig. 1(a). The GdFe was covered with a 60-nm-thick SiN cap layer. The composition of the GdFe film was determined to be $Gd_{22.5}Fe_{77.5}$ by an electron probe micro analyzer. X-ray diffraction of the film did not show any peak, suggesting that the film was amorphous. To increase the intensity of the MCP signal, 64 films were deposited layer-on-layer.

MCP measurements were performed at the BL08W beamline at SPring-8, Japan. BL08W provides circularly polarized high energy X-rays from a wiggler device [21)-22)]. The energy of the incident X-rays was 182.6 keV [23)]. The sample was set in a vacuum chamber to suppress the scattering of the X-rays by air. MCP was measured in magnetic field switching mode with a scattering angle of 178 degrees, in which the incident X-rays were parallel to the applied magnetic field. Superconducting magnets can apply magnetic fields ranging from –0.5 T to 0.5 T perpendicular to the film plane. MCP measurements were performed at 289, 250, 225, 200, 175, 150, 100, 50, and 10 K. The magnetization curves of the M_t were measured by a superconducting quantum interference device (SQUID) magnetometer. The MCP of a polycrystalline Fe plate with a thickness of 0.1 mm was measured at room temperature as a standard measurement.

Figures 1(b) and 1(c) show the magnetization curves and temperature dependence of the saturation magnetization for the remanent state of the $Gd_{22.5}Fe_{77.5}$ film, respectively. The temperature dependence of the total magnetization M_t can be written as

$$M_t(T) = |M_{t,Fe}(T)| - |M_{t,Gd}(T)|.$$
$$= M_{t,Fe}(0)\left(1 - \frac{T}{T_c}\right)^{\beta_{Fe}} - M_{t,Gd}(0)\left(1 - \frac{T}{T_c}\right)^{\beta_{Gd}}. \quad (7)$$

Here, $M_{t,Fe}(0)$ and $M_{t,Gd}(0)$ are the total magnetization of Fe and Gd at 0 K, respectively. β_{Fe} and β_{Gd} are the critical exponents of Fe and Gd, respectively, and T_c is the Curie temperature [14), 24)]. We assume $M_{t,Fe}(0)$ = 1130 emu/cm^3 [25)], β_{Fe} = 0.50 [26)]. Moreover, we determined T_c = 520 K by measuring the temperature dependence of the magnetization [14)]. It was estimated that $M_{t,Gd}(0)$ = 1161 ± 30 emu/cm^3 and β_{Gd} = 0.60 ± 0.005, leading to T_M = 131 K with Eq. (7).

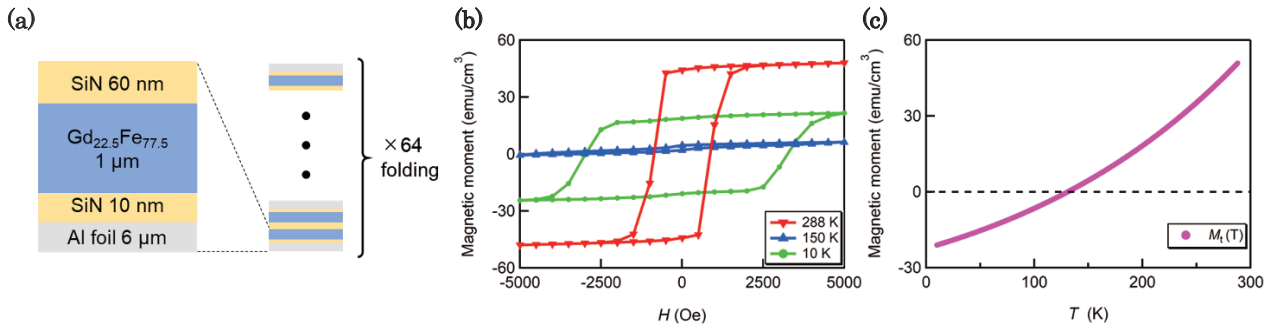

Fig. 1. (a) Structure of thin film sample used in experiment. For magnetic Compton scattering experiment, films were stacked in 64 layers to amplify signal intensity. (b) Magnetization curves at 288, 150, and 10 K. (c) Temperature dependence of saturation magnetization. Temperature at which saturation magnetization becomes zero on this curve is defined as magnetization compensation temperature T_M, and T_M = 131 K for this sample.

Figures 2(a)-2(c) show MCP as a function of the electron momentum (p_z) in atomic units (au) at 289, 150, and 10 K. The magnetic field (H = 0.5 T) was applied perpendicular to the film plane. The measurement points are indicated by the circles. The measured MCP for GdFe alloy can be reproduced by a linear combination of MCPs from 4f orbitals of Gd and those from 3d orbitals of Fe. This is because the electron orbitals of Gd from 1s to 5p and those of Fe from 1s to 3p are filled, and they are magnetically inactive and thus do not contribute to MCP. Furthermore, the contribution from the Gd 5d orbitals is negligibly small. Therefore, fitting free atom profiles to a high momentum line shape has been exploited to separate 4f contributions from 3d contributions in 4f rare earth-3d transition metal alloys [27]. The purple solid lines in Figs. 2(a)-2(c) are the best fit with the least square method based on the above assumption, and the solid blue lines and the solid red lines indicate the MCPs of Gd and Fe, respectively. The 4f contribution of Gd obtained from the literature [28] and the Fe contribution obtained from the standard measurement were used for the fitting. Above T_M, we observed that the MCP of Fe was oriented positive and the MCP of Gd was oriented negative as shown in Figs. 2(a) and 2(b) because $M_{t,Fe}(T) > M_{t,Gd}(T)$. In contrast, below T_M, we observed that the MCP of Fe was oriented negative and the MCP of Gd was oriented positive as shown in Fig. 2(c) because $M_{t,Gd}(T) > M_{t,Fe}(T)$. T_M was 131 K for this sample.

Figure 2(d) shows the temperature dependences of the spin magnetization of Fe, $M_{s,Fe}(T)$, and that of Gd, $M_{s,Gd}(T)$, calculated from the MCPs for Fe and Gd obtained by the analysis described in a previous paragraph. The smaller spin magnetizations at 100 and 150 K indicate that the magnetizations in the GdFe film were not magnetically saturated because of the small external magnetic field (≦ 0.5 T). Note that the coercive field drastically increased around T_M. Figure 2(e) shows the temperature dependence of the total spin magnetic moments, which were calculated from $M_s(T) = |M_{s,Fe}(T)| - |M_{s,Gd}(T)|$ [Eq. (7)]. Here, we assume that the spin magnetizations also follow Eq. (7). Then, the fitting indicated that $M_{s,Fe}(0)$ is 1104 ± 40 emu/cm^3 and T_S = 207 ± 5 K as shown in Fig. 2(e). Here, the measurement points at 100 K and 150 K are excluded from the fitting.

As we have determined the total magnetization M_t and the spin magnetization M_s, M_l can be obtained from Eq. (6). Figure 3 shows the temperature dependences of M_l, M_t, and M_s. Since the orbital magnetization of Gd, $M_{l,Gd}(T)$ is zero, the difference between M_t and M_s is considered to correspond to the orbital magnetization of Fe, $M_{l,Fe}$. By assuming that $M_{l,Fe}$ has the same temperature dependence as for $M_{s,Fe}(T)$, $M_{l,Fe}(0)$ is estimated to be 25 ± 2 emu/cm^3. Therefore, the ratio of the orbital magnetization to the spin magnetization in Fe is 2.2 ± 0.3 %, which is consistent with a previous study [9].

As the g-factor is given by

$$g_{Fe} = \frac{2\left(M_{s,Fe}(0)+M_{l,Fe}(0)\right)}{M_{s,Fe}(0)}, \quad (8)$$

the g-factor of Fe in the sample is estimated to be 2.04 ± 0.01 by using determined values.

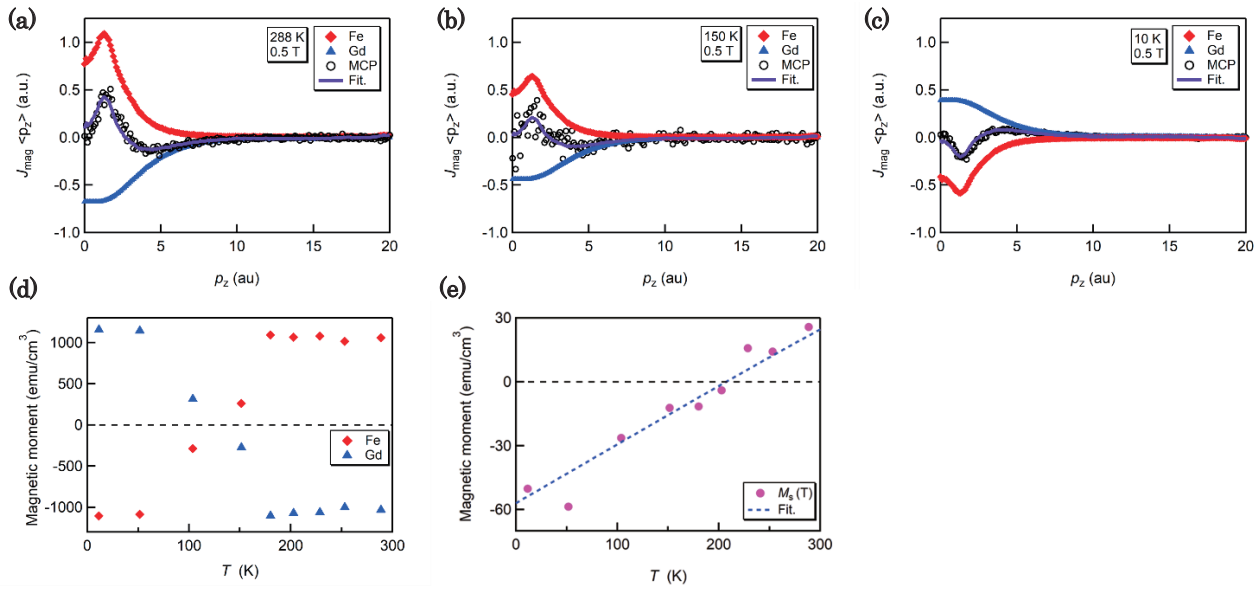

Fig. 2. (a) Magnetic Compton profiles (MCP) at 288 K, (b) 150 K, and (c) 10 K. Measurement points are indicated by circles. Solid purple lines are best fits with least square method. Red diamonds and blue triangles are deduced contributions from Fe and Gd, respectively. (d) Temperature dependences of spin magnetizations of Fe and Gd. (e) Temperature dependence of spin magnetization of GdFe. Blue dashed line represents fitting result with Eq. (7). Temperature at which spin magnetization is zero on this line is defined as spin magnetization compensation temperature T_S, and T_S = 207 ± 5 K for this sample.

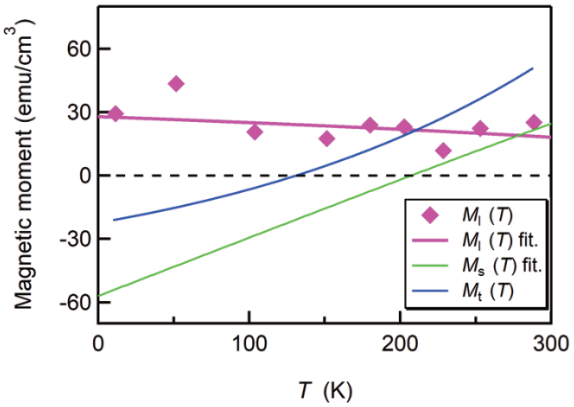

Fig. 3. Temperature dependences of orbital magnetization M_l (diamonds), spin magnetization M_S (green line), and total magnetization M_t (blue line) of GdFe. M_t was obtained by magnetization measurements using SQUID magnetometer, and M_s was determined by magnetic Compton scattering measurements.

By applying the relationship between T_A, T_M, and T_C reported in [25], the following equation is obtained for the present system,

$$T_A = \left(\frac{g_{Fe}}{g_{Gd}}\right)^{\frac{1}{\beta_{Fe}-\beta_{Gd}}} T_M + \left\{1 - \left(\frac{g_{Fe}}{g_{Gd}}\right)^{\frac{1}{\beta_{Fe}-\beta_{Gd}}}\right\} T_C. \quad (9)$$

Inserting determined values leads to $T_A = 202 \pm 2$ K, which is lower than $Ts = 207 \pm 5$ K. The small difference between T_S and T_A originate from $M_{s,Fe}(T) \gg M_{l,Fe}(T)$, $M_{t,Fe}(T) \sim M_{s,Fe}(T)$ and $M_{s,Gd}(T) = M_{t,Gd}(T)$ and it is confirmed that $T_M < T_A < T_S$ in this GdFe system.

In summary, we observed the magnetization compensation temperature and the spin magnetization compensation temperature in ferrimagnetic GdFe alloy film with perpendicular magnetic anisotropy using a SQUID magnetometer and magnetic Compton scattering. The spin magnetization and orbital magnetization of each element constituting the ferrimagnetic GdFe alloy were independently determined. Furthermore, we succeeded in estimating the angular momentum compensation temperature of the ferrimagnetic GdFe alloy film. Our results show that magnetic Compton scattering is a unique method for investigating the element specific spin magnetization and angular momentum compensation temperature in ferrimagnets.

Acknowledgements This work was supported by JSPS KAKENHI Grant Numbers JP15H05702 and JP19J21253, the Collaborative Research Program of the Institute for Chemical Research, Kyoto University, and the Cooperative Research Project Program of the Research Institute of Electrical Communication, Tohoku University. This experiment was performed with the approval of the Japan Synchrotron Radiation Research Institute (Proposal Nos. 2019A0921).

References

1) T. Jungwirth, X. Marti, P. Wadley, and J. Wunderlich: *Nat. Nanotechnol.*, **11**, 231 (2016).
2) V. Baltz, A. Manchon, M. Tsoi, T. Moriyama, T. Ono, and Y. Tserkovnyak: *Rev. Mod. Phys.*, **90**, 015005 (2018).
3) J. Železný, P. Wadley, K. Olejník, A. Hoffmann, and H. Ohno: *Nat. Phys.*, **14**, 220 (2018).
4) M. B. Jungfleisch, W. Zhang, and A. Hoffmann: *Phys. Lett. A*, **382**, 865 (2018).
5) O. Gomonay, V. Baltz, A. Brataas, and Y. Tserkovnyak: *Nat. Phys.*, **14**, 213 (2018).
6) C. D. Stanciu, A. V. Kimel, F. Hansteen, A. Tsukamoto, A. Itoh, A. Kirilyuk, and T. Rasing: *Phys. Rev. B*, **73**, 220402(R) (2006).
7) M. Binder, A. Weber, O. Mosendz, G. Woltersdorf, M. Izquierdo, J. R. Dahn, T. D. Hatchard, J.–U. Thiele, C. H. Back, and M. R. Scheinfein: *Phys. Rev. B*, **74**, 134404 (2006).
8) C. D. Stanciu, A. Tsukamoto, A. V. Kimel, F. Hansteen, A. Kirilyuk, A. Itoh, and T. Rasing: *Phys. Rev. Lett.*, **99**, 217204 (2007).
9) A. Kirilyuk, A. V. Kimel, and T. Rasing: *Rev. Mod. Phys.*, **82**, 2731 (2010).
10) A. Mekonnen, M. Cormier, A. V. Kimel, A. Kirilyuk, A. Hrabec, L. Ranno, and T. Rasing: *Phys. Rev. Lett.*, **107**, 117202 (2011).
11) A. Kirilyuk, A. V. Kimel, and T. Rasing: *Rep. Prog. Phys.*, **76**, 026501 (2013).
12) K.–J. Kim, S. K. Kim, Y. Hirata, S.–H. Oh, T. Tono, D.–H. Kim, T. Okuno, W. S. Kim, S. Kim, G. Go, Y. Tserkovnyak, A. Tsukamoto, T. Moriyama, K.–J. Lee, and T. Ono: *Nat. Mater.*, **16**, 1187 (2017).
13) S. A. Siddiqui, J. Han, J. T. Finley, C. A. Ross, and L. Liu: *Phys. Rev. Lett.*, **121**, 057701 (2018).
14) L. Caretta, M. Mann, F. Büttner, K. Ueda, B. Pfau, C. M. Günther, P. Hessing, A. Churikova, C. Klose, M. Schneider, D. Engel, C. Marcus, D. Bono, K. Bagschik, and G. S. D. Beach: *Nat. Nanotech.*, **13** (2018).
15) K. Aoshima, R. Ebisawa, N. Funabashi, K. Kuga, and K. Machida: *Jpn. J. Appl. Phys.*, **57**, 09TC03 (2018).
16) D.–H. Kim, T. Okuno, S. K. Kim, S.–H. Oh, T. Nishimura, Y. Hirata, Y. Futakawa, H. Yoshikawa, A. Tsukamoto, Y. Tserkovnyak, Y. Shiota, T. Moriyama, K.–J. Kim, K.–J. Lee, and T. Ono: *Phys. Rev. Lett.*, **122**, 127203 (2019).
17) T. Okuno, S. K. Kim, T. Moriyama, D.–H. Kim, H. Mizuno, T. Ikebuchi, Y. Hirata, H. Yoshikawa, A. Tsukamoto, K.–J. Kim, Y. Shiota, K.–J. Lee, and T. Ono: *Appl. Phys. Express*, **12**, 093001 (2019).
18) M. Imai, Y. Ogata, H. Chudo, M. Ono, K. Harii, M. Matsuo, Y. Ohnuma, S. Maekawa, and E. Saitoh: *Appl. Phys. Lett.*, **113**, 052402 (2018).
19) N. Sakai, M. Ito, H. Kawata, T. Iwazumi, M. Ando, N. Shiotani, F. Itoh, Y. Sakurai, and S. Nanao: *Nucl. Instrum. Methods A*, **303**, 488 (1991).
20) N. Sakai: *J. Appl. Crst.*, **29**, 81 (1996).
21) Y. Kakutani, Y. Kubo, A. Koizumi, N. Sakai, L. B. Ahuja, and K. B. Sharma: *J. Phys. Soc. Jpn.*, **72**, 72599 (2003).
22) M. Itou, A. Koizumi, and Y. Sakurai: *Appl. Phys. Lett.*, **102**, 082403 (2013).
23) A. Agui, A. Harako, A. Shibayama, K. Haishi, N. Tsuji, X. Liu, G. Ma, and H. Sakurai: *Journal of Magn. and Magn. Mater.*, **484** (2019).
24) Y. Hirata, D.–H. Kim, T. Okuno, T. Nishimura, D.–Y. Kim, Y. Futakawa, H. Yoshikawa, A. Tsukamoto, K.–J. Kim, S.–B. Choe, and T. Ono: *Phys. Rev. B*, **97**, 220403(R) (2018).

25) R. Hasegawa and R. Ray: *Phys. Rev. B*, **20**, 1 (1979).
26) S. Blindell: Magnetism in Condensed Matter (2001).
27) H. Sakurai, M. Ota, X. Liu, A. Morisako, Y. Sakurai, M. Itou, T. Nagao, and A. Koizumi: *J. Appl. Phys.*, **102**, 013902 (2007).
28) F. Biggs, L. B. Mendelsohn, and J. B. Mann: *Atom. Data Nucl. Data*, **16** (1975).
29) S. Mangin, C. Bellouard, S. Andrieu, F. Montaigne, P. Ohresser, N. B. Brookes, and B. Barbara: *Phys. Rev. B*, **70**, 014401 (2004).

Received Oct. 25, 2020; Accepted Nov. 19, 2020

J. Magn. Soc. Jpn., **45**, 6-11 (2021)

<Paper>

Low Current Driven Vertical Domain Wall Motion Memory with an Artificial Ferromagnet

Y. M. Hung[1], T. Li[1], R. Hisatomi[1], Y. Shiota[1], T. Moriyama[1], and T. Ono[1,2]

[1]Institute for Chemical Research, Kyoto University, *Gokasho, Uji, Kyoto 611-0011, Japan.*
[2]Center for Spintronics Research Network (CSRN), Graduate School of Engineering Science, Osaka University, *Toyonaka, Osaka 560-8531, Japan.*

We propose a new structure of vertical domain wall (DW) motion memory with artificial ferromagnet to achieve high DW controllability. The artificial ferromagnet is composed of periodically stacked ferromagnetic bilayers with relatively large and small exchange stiffness constants (A_{ex}), which refer to as strong coupling layers and weak coupling layers. By optimizing A_{ex} and the magnetic anisotropy of the weak coupling layers, DW width and position can be easily controlled. Furthermore, micromagnetic analysis shows that low critical current density for DW motion down to 2×10^{10} A/m^2 can be achieved as we increase the A_{ex} of weak coupling layers to larger than 2 pJ/m.

Key words: artificial ferromagnet, vertical domain wall motion memory, exchange stiffness constant, perpendicular magnetic anisotropy, critical current, micromagnetic analysis

1. Introduction

Domain wall (DW) motion in ferromagnetic nanowires[1] are potential candidates of future memory technologies such as racetrack memory[2)-7)], in which digital bits are stored in a series of DW, and transported through a nanowire with DW motion driven by electrical current. Since multiple DW can be compactly encoded into one ferromagnetic wire, racetrack memory promises ultra-high storage density compared with conventional magnetic memories[3),7)]. In a ferromagnetic wire-based memory cell, narrower DW indicates more digital bits can be stored. Therefore, DW width is a key factor that must be concerned. Generally, DW width (Δ) depends on the properties of ferromagnets, and can be expressed as $\Delta = \sqrt{A_{ex} / K_u}$, where A_{ex} is exchange stiffness constant and K_u is uniaxial anisotropy constant[8)]. According to previous researches, DW width is around 6.7 nm in a 15-nm-thick Co film[9)], while in a 5-nm-thick permalloy nanowire, DW width can be larger than 200 nm[10)]. The intrinsic properties of materials determine DW width, and hampers the achievement of high storage density in ferromagnetic wires. Besides, in DW motion-based technology, DW position is another key factor which needs to be precisely controlled. Currently, the approach used to control DW position is to fabricate well-designed pinning sites in nanowire[11)-13)]. However, this approach implies complicated nanofabrication is needed, and makes commercialization of DW motion memory much more difficult. Furthermore, lowering consumption power is also important for practical application of racetrack memory. Even though several approaches had been proposed to reduce critical current (J_c) for DW motion down to 10^{11} A/m[3),5),14)-15)], to attain low current driven, precisely controllable, and applicable DW motion memory with high storage density, there is still a lot of room for improvement. In this research, we propose a new structure of vertical DW motion memory with an artificial ferromagnet which is composed of periodically stacked ferromagnetic bilayers with strong and weak coupling layers. Based on this structure, we can easily reduce DW width and precisely control DW position. Micromagnetic simulations are studied to verify the feasibility of device and investigate J_c needed to drive DW motion. It is found that as we increase the A_{ex} of weak coupling layers to larger than 2 pJ/m, J_c down to 2×10^{10} A/m^2 can be achieved.

2. Memory operation scheme

Figure 1(a) shows the vertical DW motion memory proposed in this research, in which the underlayer is a heavy metal-based conduction wire, e.g., Pt, Ta, and acts as a word line for data writing. A cylindrical magnetic wire, referred to as one memory cell, is an artificial ferromagnet, which is composed of ferromagnetic multilayers with different magnetic properties. The lowermost layer of magnetic wire, colored with blue, named layer1 in Figs. 1(b) and 1(c), is set as a pinning layer with sufficiently large K_u with perpendicular magnetic anisotropy (PMA). Above layer1, the even layers, colored with green, are PMA ferromagnets with sufficiently large A_{ex} and K_u, which are referred to as strong coupling layers. The rest odd layers, colored with yellow and referred to as weak coupling layers, are non-PMA ferromagnets with sufficiently weak A_{ex}. The character of strong coupling layers is to carry storage bit, while the character of weak coupling layers is to carry DW. If the A_{ex} of weak coupling layer is sufficiently small, the smallest storage unit of one bit can be limited within a unit of one strong coupling layer (storage), and one weak coupling layer (DW). Above layer12, a set of tunnel oxide and fixed magnetic layer is connected, and acts with layer12 as a magnetic tunneling junction (MTJ)[16)-

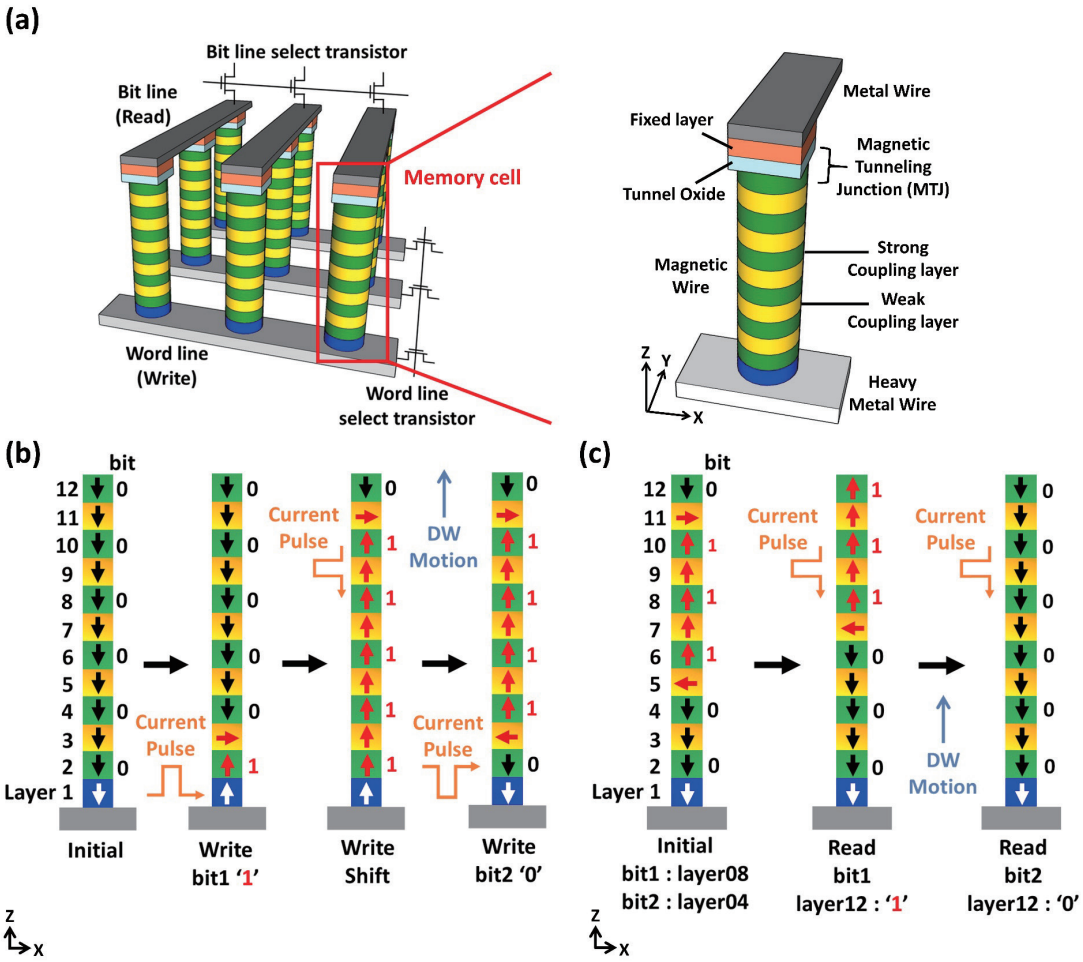

Fig. 1 (a) Illustration of vertical DW motion memory with artificial ferromagnets. Left panel: Memory array with perpendicularly arranged word line and bit line. The cylinders inside array are the multi-bit storage memory cells constructed with artificial ferromagnets. To operate a specific cylinder (cell), we can use the word line and bit line select transistors in the peripheral circuit to select the desired cell. Right panel: Detailed structure of one memory cell. (b) Data-writing scheme and (c) Data-reading scheme of the proposed memory. In (b) and (c), the numbers labeled in the left indicate layer numbers from 1 to 12, and the numbers labeled in the right of magnetic wires, next to strong coupling layers (the green layers), are the bit logic defined by magnetization of layers.

[18]. With MTJ, the logic bit performed by magnetization of layer12 can be read.

Data-writing scheme is shown in Fig. 1(b). At initial state, all layers are magnetized toward -z direction. Here, we defined -z magnetization as logic '0', and +z magnetization as logic '1'. To write bit1 '1' into magnetic wire, a current pulse is injected along x-direction into the heavy metal wire (word line). Because of the heavy metal/ferromagnet interface, a z-direction spin current is then induced and injected into magnetic wire, which can be referred to as spin Hall effect[19]. The injected spin current results in spin-orbit torque (SOT) inside ferromagnetic layers, and thus switches layer1 and layer2 toward +z direction. This switching process of SOT had been widely studied in magnetic memories[19)-21)]. When layer1 and layer2 switched, the weak coupling layer3 performs like a DW in the artificial ferromagnet as shown in Fig. 1(b). After writing, write shift process is needed to move bit1 to other storage layer. In this process, -z-direction current pulses (J) are injected into magnetic wire and drive DW upward with spin transfer torque (STT)[22]. As bit1 reached the storage layer (layer8 shown in Fig. 1(b)), the weak coupling layer - layer9, performs as a new DW. To write bit2 '0' into magnetic wire, a negative current pulse is injected along x-direction into the heavy metal wire, and switched layer2 downward again. After the writing of bit2, another DW in layer3 is nucleated, and another write shift process will be executed to move bit2 to the storage layer. Data reading scheme is shown in Fig. 1(c). Similar to the write shift process, -z-direction current pulses are injected to drive DW, and shift the program bit to layer12 for reading by MTJ. Here, we assume that bit2 had already be shifted to layer4, and thus bit1 was shifted to layer10, at initial state. To read bit1, a current pulse is needed to shift bit1 to layer12, and logic '1' inside layer12 can be read. Likewise, as more pulses are injected, bit2 can also be shifted to layer12, and the logic '0' of bit2 can be read.

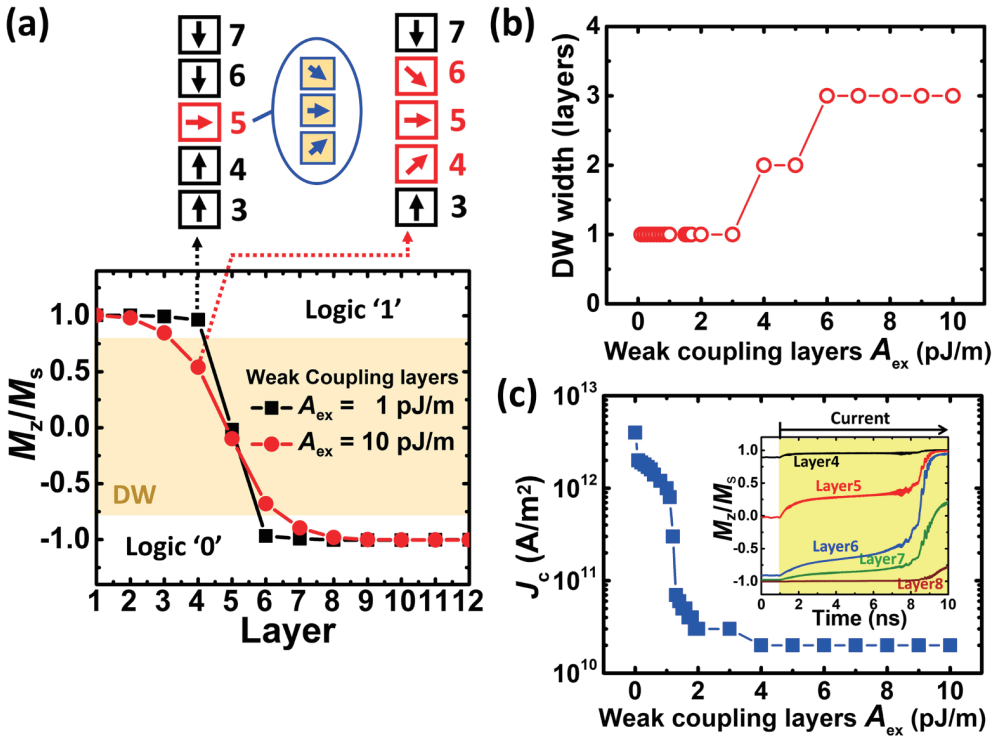

Fig. 2 (a) The z-axis magnetization of 12 layers with weak coupling layers A_{ex} = 1 pJ/m and 10 pJ/m after magnetization relaxation. The insets in upper panel illustrate the magnetization of layers near DW layer. The DW layers are colored with red, while the inset connected with layer5 in the case of A_{ex} = 1 pJ/m shows the magnetization of three magnetic cells inside layer5. (b) DW widths counted with layers and (c) J_c needed to drive the program bit from layer5 to layer7, as a function of A_{ex} of weak coupling layers. The inset of (c) illustrates z-axis magnetization change from layer4 to layer8 as a function of time in the case of weak coupling layers A_{ex} = 2 pJ/m. A 10 ns, $J = J_c = 3 \times 10^{10}$ A/m² current pulse is injected from 1 ns (yellow area), and cause the switching of layer5, layer6, and layer7.

The proposed scheme suggests that DW position can always be controlled in the weak coupling layers and the program bits are carried only by the strong coupling layers. By using this structure, we can effectively control DW position and achieve high storage density in magnetic wire. It should be noticed that the data-reading scheme of this memory is destructive, in which the storage bits disappear after the reading process. Therefore, a write-after-read architecture[23], or well-positioned reading heads (MTJ) is suggested for the actual application. Here, we focus on the feasibility of the proposed structure by using micromagnetic analysis.

3 Micromagnetic analysis

3.1 Parameters setting

To verify the feasibility of vertical DW motion memory, micromagnetic simulations were performed in Mumax3 3.10, a GPU-accelerated simulation program[24]. In our simulation, 12 layers in a vertical magnetic wire were constructed, as introduced in Fig. 1. The magnetic wire of artificial ferromagnet is a cylinder with 20 nm-diameter and the thickness of each layer is 3 nm. The size of magnetic cells is defined as a 1 nm × 1 nm × 1 nm cube. Therefore, 3 cells are included inside one layer along z-axis direction. The A_{ex} and K_u of each layer used in this work are summarized in table 1. Layer1 is with $K_u = 10^7$ J/m³, and A_{ex} =10 pJ/m as a pinning layer. Even layers from layer2 to layer12 are strong coupling layers, with $K_u = 10^6$ J/m³ and A_{ex} = 10 pJ/m, based on the reference[25]. Odd layers from layer3 to layer11 are weak coupling layers without PMA, in which K_u = 0 J/m³, and A_{ex} with 0-10 pJ/m are assigned. The A_{ex} between strong and weak coupling layers is calculated by the harmonic means of those of the strong and weak coupling layers[24]. Saturation magnetization (M_s) and Gilbert damping constant (α) are 8×10^5 A/m and 0.01, respectively[25]. The initial magnetization from layer1 to layer4 are set with +z, while layer6 to layer12 are set with -z. DW is assigned in layer5. After the setting, magnetization relaxation was then executed to see if DW could be controlled in weak coupling layer in steady state.

3.2 Domain wall position and thickness

The magnetization of each layer with weak coupling layers A_{ex} = 1 pJ/m and 10 pJ/m after magnetization relaxation are shown in Fig. 2(a). To derive DW width, we defined DW as the layers with z-axis reduced magnetization (M_z/M_s) ranged from -0.75 to 0.75, as the

yellow area labeled in Fig. 2(a). In the case of A_{ex} = 1 pJ/m, DW is limited only at layer5 after relaxation, which indicates that it is possible to control DW position within weak coupling layers. Besides, in the case of A_{ex} = 10 pJ/m, DW width is enlarged to 3 layers from layer4 to layer6. These results suggest that DW width can be controlled by assigning different A_{ex} of weak coupling layers. Since DW width Δ can be expressed as $\Delta \propto \sqrt{A_{ex}}$[8], it is expected that higher A_{ex} results in the larger DW width. The correlation of DW width and the A_{ex} of weak coupling layers is exhibited in Fig. 2(b). If the A_{ex} of weak coupling layers is optimized to smaller than 3 pJ/m, DW width can be controlled only inside one layer. The narrower DW width promises that more storage unit can be stacked in memory cells under the same aspect ratio, which indicates higher storage density of one memory cell can be achieved under the same process limitation.

Table 1 A_{ex} and K_u of 12 layers used in this work.

Layer Name	Layer Number	A_{ex} (pJ/m)	K_u (J/m^3)
Pinning layer	1	10	10^7
Strong coupling layer	2, 4, 6, 8, 10, 12	10	10^6
Weak coupling layer	3, 5, 7, 9, 11	0-10	0

3.3 Critical current density study

Critical current density J_c needed to drive DW motion are also studied. In this research, J_c is defined as the lowest current density for driving DW from layer5 to layer7 under a 10 ns-long current pulse. To verify J_c, firstly, DW was assigned in layer5, and magnetization relaxation was executed. After relaxation, M_z/M_s of each layer was then measured from 0 ns. At the time t = 1 ns, a 10 ns current pulse was injected into magnetic wire along -z-direction, as exhibited in reading scheme shown in Fig. 1(c). When the current pulse injection finished at t = 11 ns, we examined whether M_z/M_s of layer5 and layer6 can be switched to larger than 0.75. The lowest current density that can drive the switching was then extracted as J_c. The non-adiabaticity of STT[22),24)] is set as zero, and only the adiabatic torque[22)] is considered in our analysis. The M_z/M_s dynamics from layer4 to layer8 as a function of time in the case of A_{ex} = 2 pJ/m under a 10 ns current pulse with $J = J_c = 3 \times 10^{10}$ A/m^2 is shown in the inset of Fig. 2(c). At the beginning, M_z/M_s of layer5 was around 0, and performed as a DW. Layer6 and layer7 were magnetized downward. When the current pulse was injected at 1 ns (see the yellow area), layer5, layer6, and layer7 started to switch upward. At t = 9 ns, the M_z/M_s of layer5 and layer6 were all larger than 0.75, which means that layer5 and layer6 are switched by the current pulse. At the meanwhile, M_z/M_s of layer7 reached around 0, and became a new DW. With a current pulse with $J = J_c$, DW can be successfully shifted from layer5 to layer7. Figure 2(c) shows the J_c as a function of the A_{ex} of weak coupling layers. It can be noticed that a prominent drop of J_c occurs when A_{ex} increases from 1 pJ/m to 2 pJ/m. As A_{ex} increases to larger than 2 pJ/m, J_c can be reduced down to 2×10^{10} A/m^2, and shows almost no A_{ex} dependence from 2 to 10 pJ/m. The results above suggest that, by optimizing A_{ex} and K_u of the bilayers in artificial ferromagnet, for example, with the given parameters in our simulations with A_{ex} of weak coupling layers from 2 to 3 pJ/m, it is promising to obtain narrow DW width, controllable DW position, and also low current driven properties simultaneously.

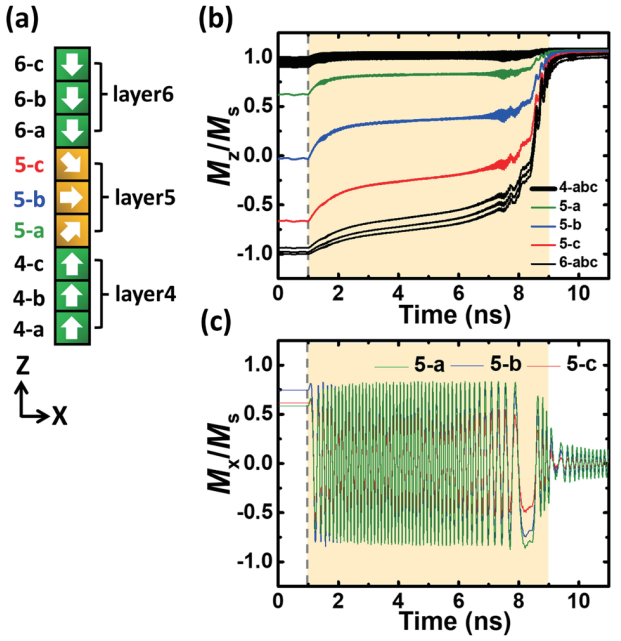

Fig. 3 (a) Illustration of the cells from layer4 to layer6 in the simulation of this work. The icons labeled in the left are the name of cells. The arrows inside the cells are magnetization after relaxation. DW is assigned in the three cells of layer5. (b) Time dependent dynamics of M_z/M_s and (c) M_x/M_s of the cells from layer4 to layer6 in the case of A_{ex} = 2 pJ/m under $J = J_c = 3 \times 10^{10}$ A/m^2. The gray dash line and the yellow area labeled in (b)(c) indicates the time current pulse was injected and time interval that layer5 and layer6 switched.

3.4 Discussions

To specify the dynamics of DW motion in artificial ferromagnet-based magnetic wire, we firstly study switching behaviors of the cells from layer4 to layer6. In our simulations, the thickness of each layer is 3 nm and the size of micromagnetic cell is a 1 nm-sized cube. Therefore, for each layer, 3 cells along z-axis are included, as labeled with a, b, c of every layers shown in Fig. 3(a). In this analysis, DW was initially assigned in layer5, and magnetization relaxation was then executed. Current pulse was injected at t = 1 ns, like the measurement used to study J_c. Reduced magnetization along z-axis and x-

axis (M_x/M_s) of the cells from layer4 to layer6 in the case of weak coupling layers A_{ex} = 2 pJ/m under $J = J_c = 3 \times 10^{10}$ A/m^2 correlated with time are shown in Figs. 3(b) and 3(c). Here, we should notice that the magnetization of each cell shown in Fig. 3 is the average magnetization of the cells in its xy plane. For example, the magnetization of cell 5-b indicates the average magnetization of the cells in cell 5-b plane. From Fig. 3(b), when current pulse was injected at t = 1 ns (see the yellow area), the cells of layer5 and layer6 started to switch upward. At t = 9 ns, all of the cells in layer5 and layer6 magnetized toward +z, and the switching process finished. The magnetization precession in the xy plane of cell 5-a, 5-b, and 5-c can be observed from the M_x/M_s shown in Fig. 3(c). When current pulse was injected, the cells started to precess. As current induced STT became large enough to overcome the damping torque[22], all magnetization of the cells switched upward. The switching can be figured out as a DW depinning process[25]. Therefore, we can conclude that, if A_{ex} of weak coupling layers is sufficiently large (> 2 pJ/m), DW motion memory based on the artificial ferromagnet can be attained.

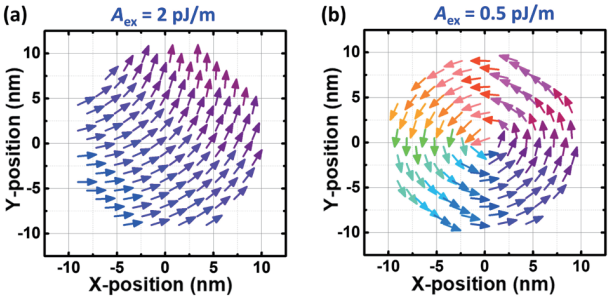

Fig. 4 Magnetization distribution of cells in cell 5-b plane in the case of (a) A_{ex} = 2 pJ/m and (b) A_{ex} = 0.5 pJ/m after magnetization relaxation and without current injection. XY coordinate indicates the position of each cell in cell 5-b plane since the xy cross-section of our device is a circle with 20 nm-diameter.

The abrupt J_c drop as A_{ex} of weak coupling layers increase from 1 pJ/m to 2 pJ/m shown in Fig. 2(c) is the phenomenon beyond our comprehension. To understand the underlying physics, we study magnetization distribution of cell 5-b plane in the DW layer - layer5, in different A_{ex} cases. The magnetization vector maps of the cell 5-b plane after magnetization relaxation in the case of A_{ex} = 2 pJ/m ($J_c = 3 \times 10^{10}$ A/m^2) and A_{ex} = 0.5 pJ/m ($J_c = 1.6 \times 10^{12}$ A/m^2) are shown in Fig. 4. Since the cells in cell 5-b plane are in the center of layer5 along z-axis, magnetization of cells in cell 5-b plane always direct perpendicularly to z-axis, as illustrated in Fig. 3(a). Hence, the z-axis magnetization can be neglected. In Fig. 4(a), it is exhibited that, at A_{ex} = 2 pJ/m, the magnetization of cells in cell 5-b plane performs as a single domain structure[26]. We can infer that STT acts only toward one direction as current pulse is injected. The STT in this case is quite efficient and small current injection is enough to drive DW. Therefore, small J_c can be attained. On the other hand, if A_{ex} of weak coupling layers is too small, like the A_{ex} = 0.5 pJ/m case shown in Fig. 4(b), the magnetization of cells in DW layer perform as a vortex structure[27),28]. In this case, STT is cancelled out in DW layer. The switching process could be achieved only if injected current is sufficiently large to break the symmetry of magnetization. Therefore, we can conclude that the abrupt J_c drop from A_{ex} = 1 pJ/m to 2 pJ/m shown in Fig. 2(c) is resulted from the transition of magnetization in DW layer from vortex into single domain structure because of sufficiently large intra-layer exchange coupling of weak coupling layers. Besides, as A_{ex} increases from 2 to 10 pJ/m, since single domain structure in DW layer is already achieved, no apparent dependence between J_c and A_{ex} can be observed.

4. Conclusion

In summary, we proposed a new structure of vertical DW motion memory with artificial ferromagnet that composed of periodic bilayers with different exchange stiffness constants A_{ex} and uniaxial magnetic anisotropy energy constants K_u in this research. Based on the structure, we can simply manipulate DW position within the weak coupling layers and also minimize DW width by tuning A_{ex} and K_u of the individual layer. Furthermore, micromagnetic analysis suggests that A_{ex} larger than 2 pJ/m in weak coupling layers can effectively reduce critical current density J_c down to 2×10^{10} A/m^2, which can be explained by the transition of magnetization in DW layer from vortex into single domain structure because sufficiently large intra-layer exchange coupling of weak coupling layers are achieved.

The artificial ferromagnet-based structure proposed in our research provides several advantages compared with conventional DW motion memories[2)-7)]. First, to precisely control DW position, what we should do in this structure is to fabricate appropriate periodical bilayers with simple film deposition instead of complicated processes for making pinning sites[11)-13)]. This suggests high feasibility of commercialization. Second, since the artificial ferromagnet is composed of bilayers with different magnetic properties, the parameters of weak and strong coupling layers can be adjusted separately, which means that we can optimize the layers for program bit and DW according to their own device requirements. Therefore, it is simple to narrow the DW width by tuning the parameters in weak coupling layers without affecting the properties of strong coupling layers. To select appropriate materials for the artificial ferromagnet, one can choose the traditional ferromagnet, such as Co, or Ni, as strong coupling layers. Weak coupling layers can be fabricated with the alloys of ferromagnet and non-magnetic metals, for example, CoPt, or CoCu, and the DW properties can be tuned by adjusting the atomic percentage of alloys. It

is much simpler to optimize total performance of device on this structure than on traditional ones. Third, the proposed structure shows prominently low current driven properties as sufficiently high A_{ex} of weak coupling layers can be achieved. These evidences indicate that artificial ferromagnet-based structure is prospective to achieve low power consumption, precisely controllable, high storage density DW motion memory, and furthermore, as a promising candidate to speed up the commercialization of DW motion memory.

Acknowledgements This work was partly supported by JSPS KAKENHI (Grant numbers JP15H05702, JP18K19021, JP18H01859, JP17H04924, JP19K21972, JP20H00332, JP20K15161, and 18J22219), and Collaborative Research Program of the Institute for Chemical Research, Kyoto University.

References

1) T. Ono, H. Miyajima, K. Shigeto, K. Mibu, N. Hosoito and T. Shinjo, *Science*, **284**, 468 (1999).
2) S. Parkin, M. Hayashi, and L. Thomas, *Science*, **320**, 190 (2008).
3) S. Parkin, and S.-H. Yang, *Nat. Nanotechnol.*, **10**, 195 (2015).
4) H.-P. Trinh, W. Zhao, J.-O. Klein, Y. Zhang, D. Ravelsona, and C. Chappert, *IEEE Trans. Circuits Syst.*, **60**, 1469 (2013).
5) D. Bang, P. V. Thach, and H. Awano, *J. Sci. Adv. Mater. Dev.*, **3**, 389 (2018).
6) Y. Zhang, X. Zhang, J. Hu, J. Nan, Z. Zheng, Z. Zhang, Y. Zhang, N. Vernier, D. Ravelosona, and W. Zhao, *Sci. Rep.*, **6**, 35062 (2016).
7) W. S. Zhao, Y. Zhang, H.-P. Trinh, J.-O. Klein, C. Chappert, R. Mantovan, A. Lamperti, R. P. Cowburn, T. Trypiniotis, M. Klaui, J. Heinen, B. Ocker, and D. Ravelosona, *Magnetic domain-wall racetrack memory for high density and fast data storage* (IEEE, 2012).
8) P. Chureemart, R. F. L. Evans, and R. W. Chantrell, *Phys. Rev. B*, **83**, 184416 (2011).
9) L. Thomas, M. G. Samant, and S. S. P. Parkin, *Phys. Rev. Lett.*, **84**, 1816 (2000).
10) D. Atkinson, D. A. Allwood, C. C. Faulkner, G. Xiong, M. D. Cooke, and R. P. Cowburn, *IEEE T. Magn.*, **39**, 2663 (2003).
11) T. Ono, H. Miyajima, K. Shigeto and T. Shinjo, *Appl. Phys. Lett.*, **72**, 1116 (1998).
12) H. Tanigawa, K. Kondou, T. Koyama, K. Nakano, S. Kasai, N. Ohshima1, S. Fukami, N. Ishiwata, and T. Ono, *Appl. Phys. Express*, **1**, 011301 (2008).
13) T. Koyama, G. Yamada, H. Tanigawa, S. Kasai, N. Ohshima, S. Fukami, N. Ishiwata, Y. Nakatani, T. Ono, *Appl. Phys. Express*, **1**, 101303 (2008).
14) D. Ravelosona, S. Mangin, J. A. Katine, Eric E. Fullerton, and B. D. Terris, *Appl. Phys. Lett.*, **90**, 072508 (2007).
15) Z. Meng, S. He, L. Huang, J. Qiu, T. Zhou, C. Panagopoulos, G. Han, and K.-L. Teo, *Appl. Phys. Lett.*, **109**, 142403 (2016).
16) N. Nishimura, T. Hirai, A. Koganei, T. Ikeda, K. Okano, Y. Sekiguchi, and Y. Osada, *J. Appl. Phys.*, **91**, 5246 (2002).
17) S. Ikeda, J. Hayakawa, Y. M. Lee, F. Matsukura, Y. Ohno, T. Hanyu, and H. Ohno, *IEEE Trans. Electron. Devices*, **54**, 991 (2007).
18) S. Ikeda, K. Miura, H. Yamamoto, K. Mizunuma, H. D. Gan, M. Endo, S. Kanai, J. Hayakawa, F. Matsukura, and H. Ohno, *Nat. Mater.*, **9**, 721 (2010).
19) L. Lu, O. J. Lee, T. J. Gundmundsen, D. C. Ralph, and A. Buhrman, *Phys. Rev. Lett.*, **109**, 096602 (2012).
20) S. Fukami, T. Anekawa, C. Zhang, and H. Ohno, *Nat. Nanotechol.*, **11**, 621 (2016).
21) T. Moriyama, W. Zhou, T. Seki, K. Takanashi, and T. Ono, *Phys. Rev. Lett.*, **121**, 167202 (2018).
22) A. Brataas, A. D. Kent, and H. Ohno, *Nat. Mater.*, **11**, 372 (2012).
23) R. E. Jones Jr., P. D. Maniar, R. Moazzami, P. Zurcher, J. Z. Witowski, Y.T.Lii, P.Chu, and S. J. Gillespie, *Thin Solid Films*, **270**, 580, (1995).
24) A. Vansteenkiste, J. Leliaert, M. Dvornik, M. Helsen, F. Garcia-Sanchez, and B. V. Waeyenberge, *AIP Adv.*, **4**, 107133 (2014).
25) C. Yoshida, T. Tanaka, T. Ataka, and A. Furuya, *IEEE T. Magn.*, **55**, 3401105 (2019).
26) J. Shibata, G. Tatara, and H. Kohno, *J. Phys. D: Appl. Phys.*, **44**, 384004 (2011).
27) C. L. Dennis, R. P. Borges, L. D. Buda, U. Ebels, J. F. Gregg, M. Hehn, E. Jouguelet, K. Ounadjela, I. Petej, I. L. Prejbeanu, and M. J. Thornton, *J. Phys.: Condens. Mater.*, **14**, 1175 (2002).
28) T. Shinjo, T. Okuno, R. Hassdorf, K. Shigeto, and T. Ono, *Science*, **289**, 930 (2000).

Received Aug. 20, 2020; Accepted Sep. 25, 2020

Journal of the Magnetics Society of Japan

Vol. 45 No. 1 (通巻第313号) 2021年1月1日発行

Vol. 45 No. 1 Published Jan. 1, 2021
by the Magnetics Society of Japan
Tokyo YWCA building Rm207, 1–8–11 Kanda surugadai, Chiyoda-ku, Tokyo 101–0062
Tel. +81–3–5281–0106 Fax. +81–3–5281–0107

Printed by JP Corporation Co., Ltd.
Sports Plaza building 401, 2–4–3, Shinkamata Ota-ku, Tokyo 144–0054
Advertising agency: Kagaku Gijutsu-sha

発行：（公社）日本磁気学会 101–0062 東京都千代田区神田駿河台 1–8–11 東京YWCA会館 207 号室
製作：ジェイピーシー 144–0054 東京都大田区新蒲田 2–4–3 スポーツプラザビル401 Tel.（03）6715–7915
広告取扱い：科学技術社 111–0052 東京都台東区柳橋 2–10–8 武田ビル4F Tel.（03）5809–1132